

Building Blocks of Planet Formation

Ziyao Xiong

Abstract—This study examines planetesimal formation in protoplanetary discs. Simulations of dust settling under advective dynamics reveal that settling timescales decrease with radial distance R and remain below 1 Myr beyond 50 AU, enabling planetesimal formation in outer regions. To include turbulence, the advection-diffusion equation was solved, yielding a turbulence strength parameter $\alpha \sim 10^{-4}$, consistent with observations. Particle sizes required for settling were also analyzed, showing that the size decreases with R and must reach $10^{-2} \sim 10^{-1}$ m scales to overcome turbulent diffusion.

I. INTRODUCTION

THE formation of planetesimals, kilometer-scale precursors to planets, is fundamental to understanding planetary system development. Protoplanetary discs, composed primarily of hydrogen and helium gas with dust from supernova remnants, provide the environment for dust aggregation, where sub-micron grains collide, stick, and settle toward the mid-plane under gravity. Observations, such as ALMA imaging of HL Tau, reveal structures suggestive of planetesimal growth but do not resolve the mechanisms of dust aggregation and settling [1]. Addressing these gaps, this study examines dust settling dynamics using advection-diffusion equation, where the conditions (timescales, dust sizes) for dust-to-gas density ratios exceeding 1 is analyzed and the turbulence strength (α) is calibrated with observations. Numerical solutions employ upwind schemes for advection and central differencing for diffusion. This work offers insights into dust dynamics and growth processes critical to planetesimal formation.

II. THEORY

Protoplanetary discs are modeled as cylinders in cylindrical coordinates (R, ϕ, z) , as shown in Fig. 1.

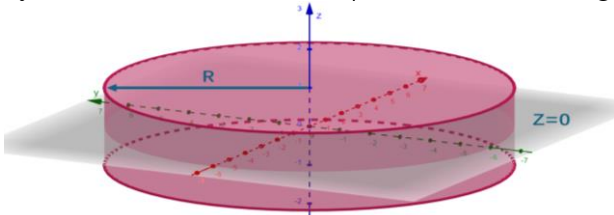


Fig.1. The flat, cylindrical, symmetric structure of the disc. R represents the radial distance from z -axis.

These discs form during the collapse of a molecular cloud, where the conservation of angular

momentum creates axisymmetric structures with physical properties largely independent of ϕ . Thus, this study focuses on variations in R and z only. In the vertical (z) direction, the central star's gravity compresses material toward the mid-plane, while gas thermal pressure counteracts this compression. This balance establishes hydrostatic equilibrium, resulting in a symmetric density distribution at the mid-plane. Hydrostatic equilibrium is expressed as:

$$\frac{1}{\rho_g} \frac{\partial P}{\partial z} = - \frac{GMz}{(R^2 + z^2)^{3/2}}, \quad (1)$$

where the LHS represents the vertical pressure gradient, the RHS corresponds to the vertical gravitational force density exerted by the central star. Here, G is the gravitational constant, M is the mass of the star. For thin discs ($z \ll R$), the gravitational term simplifies to:

$$\frac{1}{\rho_g} \frac{\partial P}{\partial z} \approx -\Omega^2 z, \quad \Omega = \sqrt{\frac{GM}{R^3}}, \quad (2)$$

where Ω is the Keplerian angular frequency.

The pressure P is related to the gas density ρ_g and the sound speed c_s by the ideal gas law:

$$P = \rho_g c_s^2, \quad c_s = \sqrt{\frac{k_b T(R)}{2m_H}}, \quad T(R) = 264 \text{ K} \left(\frac{R}{1 \text{ AU}} \right)^{-1/2}, \quad (3)$$

where m_H is the mass of a hydrogen atom. c_s quantifies the propagation speed of pressure disturbances in the gas, which increases with temperature, T . Thus, the disc's hotter regions have stronger thermal pressure support against gravity. T decreases with R due to heating from the central star. Substitute Equation (3) into Equation (2) and solve for the vertical density profile gives:

$$\rho_g(z) = \rho_g(R, z=0) \exp\left(-\frac{z^2}{2H^2}\right), \quad H = \frac{c_s}{\Omega}, \quad (4)$$

where $\rho_g(R, z=0)$ is the mid-plane density, and H is the scale height of the disc. Physically, H reflects the balance between thermal pressure, determined by c_s , and gravitational pull, governed by Ω . The further from the star, the larger H becomes, as thermal confinement decreases slower than gravitational confinement with R .

$\rho_g(R, z=0)$ decreases with R , following:

$$\rho_g(R, z=0) = 5 \times 10^{-7} \text{ kg m}^{-3} \left(\frac{R}{1 \text{ AU}} \right)^{-3}. \quad (5)$$

The steep power-law index (-3) arises as the gas mass is concentrated closer to the star, where the gravitational pull is stronger.

The advection equation describing the motion of dust particles under turbulence-free conditions, is

derived from the mass conservation. The dust mass M_d within a small volume ΔV is given by:

$$M_d = \iiint \rho_d dV, \quad (6)$$

where ρ_d is the dust density. The rate of change in M_d must equal the net flux across the boundaries of the volume. In the vertical direction (z) relevant to this study, its differential form is expressed as:

$$\frac{\partial \rho_d}{\partial t} + \frac{\partial}{\partial z} (u_z \rho_d) = 0, \quad (7)$$

where u_z is the vertical velocity of the dust particles. Under the terminal velocity approximation, it is assumed that dust particles reach a steady state in a short time t_s , where the gravitational force pulling the particles toward the mid-plane and the drag force exerted by the surrounding gas balance. The gravitational force F_g derived from Equation (2) and the opposing drag force is expressed as:

$$F_g = -m\Omega^2 z = F_{\text{drag}} = m \frac{u_z}{t_s}, \quad t_s = \sqrt{\frac{\pi \rho_{\text{in}} a}{8 \rho_g c_s}}. \quad (8)$$

where ρ_{in} is the internal density of the dust particle. Solving Equation (8) yields:

$$u_z = -\Omega^2 z t_s. \quad (9)$$

The negative sign indicates that the velocity is directed toward the mid-plane.

In a more complete picture, protoplanetary discs are turbulent, where turbulence acts as an effective diffusion mechanism, preventing dusts from fully concentrating in the mid-plane. Turbulence diffuses dusts away and maintains a broader distribution of dusts. The dust's diffusive flux can be modeled using Fick's law [2] and Shakura-Sunyaev α -disc model [3] as:

$$J_{\text{diffusion}} = -D \rho_g \nabla \left(\frac{\rho_d}{\rho_g} \right), \quad D = \alpha c_s H, \quad (10)$$

where D is the turbulent diffusivity and the dimensionless parameter α represents its strength.

Thus, with diffusion, Equation (7) is modified to:

$$\frac{\partial \rho_d}{\partial t} + \frac{\partial}{\partial z} (u_z \rho_d) - D \frac{\partial}{\partial z} \left[\rho_g \frac{\partial}{\partial z} \left(\frac{\rho_d}{\rho_g} \right) \right] = 0. \quad (11)$$

III. METHODS

Physical quantities can be normalized by their reference values and become dimensionless to simplify calculations. As shown in Fig. 2, the parameters H , T , c_s , Ω and ρ_g ($R, z=0$) vary significantly with R , making global reference values unsuitable. Thus, reference values are defined locally at each R , eliminating R 's unit from the equations and retaining only the intrinsic units of these quantities as references. The reference time is chosen as Ω^{-1} , the orbital timescale in a Keplerian disc, while the vertical coordinate z is expressed in multiples of H_{ref} , the characteristic vertical scale height of the disc. Table 1

summarizes the reference values and natural forms of the quantities used.

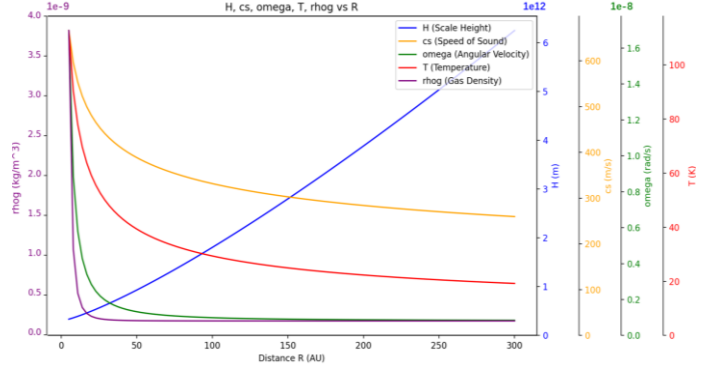


Fig. 2. Profiles of Ω , c_s , ρ_g , H as a function of R . ρ_g decreases the most rapidly, Ω also exhibits a steep decline, and c_s decreases more gradually. H increases with R .

TABLE 1

	Reference value	Unit	Natural form
R	$R_{\text{ref}} = R_{\text{ref}}$	m	$\tilde{R} = 1$
T	$T_{\text{ref}} = T(R_{\text{ref}})$	K	$\tilde{T} = 1$
c_s	$c_{s,\text{ref}} = c_s(T_{\text{ref}})$	m/s	$\tilde{c}_s = 1$
Ω	$\Omega_{\text{ref}} = \Omega(R_{\text{ref}})$	s^{-1}	$\tilde{\Omega} = 1$
H	$H_{\text{ref}} = c_{s,\text{ref}}/\Omega_{\text{ref}}$	m	$\tilde{H} = 1$
z	H_{ref}	m	$\tilde{z} H_{\text{ref}} = z$
ρ_{g0}	$\rho_{g0,\text{ref}} = \rho_{g0}(R_{\text{ref}})$	kg/m^3	$\tilde{\rho}_{g0} = 1$
ρ_g	$\rho_{g0,\text{ref}}$	kg/m^3	$\tilde{\rho}_g = e^{-\tilde{z}^2/2}$
ρ_d	$\rho_{g0,\text{ref}}$	kg/m^3	$\rho_{g0,\text{ref}} \tilde{\rho}_d = \rho_d$
t	$t_{\text{ref}} = \Omega_{\text{ref}}^{-1}$	s	$\tilde{t} t_{\text{ref}} = t$
t_s	t_{ref}	s	$\tilde{t}_s = \sqrt{\frac{\pi}{8}} \frac{\Omega_{\text{ref}} \rho_{\text{in}} a}{\tilde{\rho}_g \rho_{g0,\text{ref}} \tilde{c}_s c_{s,\text{ref}}} = k e^{\tilde{z}^2/2}$
u_z	$\frac{u_{z,\text{ref}}}{\Omega_{\text{ref}}^2 t_{\text{ref}} H_{\text{ref}}} = c_{s,\text{ref}}$	m/s	$\tilde{u}_z = -\tilde{t}_s \tilde{z}$ $= -k \tilde{z} e^{\tilde{z}^2/2}$
D	$D_{\text{ref}} = c_{s,\text{ref}} H_{\text{ref}}$	NA	$\tilde{D} = \alpha$

A. Pure Advection Situation

Writing Equation (7) to its natural form yields:

$$\frac{\partial \rho_d}{\partial t} = \frac{\rho_{\text{ref}}}{t_{\text{ref}}} \frac{\partial \tilde{\rho}_d}{\partial \tilde{t}} = \frac{\partial}{\partial z} (u_z \rho_d) = \frac{u_{z,\text{ref}} \rho_{\text{ref}}}{H_{\text{ref}}} \frac{\partial}{\partial \tilde{z}} (\tilde{u}_z \tilde{\rho}_d), \quad (12)$$

where $u_{z,\text{ref}}/H_{\text{ref}} = \Omega_{\text{ref}} = 1/t_{\text{ref}}$. Therefore, the coefficients in front of the time-derivative term and the space-derivative term can be eliminated, resulting in:

$$\frac{\partial \tilde{\rho}_d}{\partial \tilde{t}} + \frac{\partial}{\partial \tilde{z}} (\tilde{u}_z \tilde{\rho}_d) = 0. \quad (13)$$

This can be written in a flux-conservative form:

$$\frac{\partial \tilde{\rho}_d}{\partial \tilde{t}} = -\frac{\partial \tilde{F}}{\partial \tilde{z}}, \quad \text{where } \tilde{F} = \tilde{u}_z \tilde{\rho}_d, \quad (14)$$

Equation (14) can be solved by discretizing time and space on a 2D grid with constant spacing. Dust flows downward toward lower z , therefore, the flux at a grid point i depends on the upstream flux at the point $i+1$. To align with this physical direction of information propagation, an upwind method uses the upstream value to compute the flux at i is used:

$$(\rho_d^{n+1,i} - \rho_d^{n,i})/\Delta t = -u_{z,i+1}\rho_d^{n,i+1} - u_{z,i}\rho_d^{n,i}/\Delta z, \\ \rho_d^{n+1,i} = \rho_d^{n,i} - \frac{\Delta t}{\Delta z}(u_{z,i}\rho_d^{n,i+1} - u_{z,i-1}\rho_d^{n,i}). \quad (15)$$

Since u_z is varying with z , we apply the “frozen coefficient” method to evaluate the numerical stability of Equation (15). Hold each grid point i with constant $u_z(i)$ and performs a von Neumann analysis locally, the local CFL condition $|u_z(i)\Delta t/\Delta z| \leq 1$ can be derived. Therefore, imposing a global CFL condition $\max|u_z(i)|\Delta t/\Delta z \leq 1$ ensures that all local conditions are met, thus achieving stability across the entire computational domain. As $|u_z(i)|$ increases with z , $\max|u_z(i)|$ can be calculated from the maximum z value of our interest.

We only analyze the upper plane ($z=0$ to $z=3H$) due to disc’s symmetry, simplifying calculations. At $z=3H$ ($\tilde{z}=3$), ρ_g drops to 1.1% of its mid-plane value, and dust, 1% of ρ_g , further reduces to 0.011%, making its contribution negligible. Beyond $z=3H$, at larger radii like $R=100$ AU ($H/R \sim 0.1$), z/R becomes significant, violating the $z \ll R$ assumption. This is also why our simulation range is restricted to $R \leq 100$ AU.

It is worth noticing that at the $z=0$ boundary, contributions come from both the upper and lower planes. Using a forward upwind method for the lower plane (as u_z reverses), $\rho_d^{1,0}$ is computed as:

$$\rho_d^{1,0} = \rho_d^{0,0} - \frac{\Delta t}{\Delta z}(F^{0,1} - F^{0,0}) - \frac{\Delta t}{\Delta z}(F^{0,0} - F^{0,-1}) = \\ \rho_d^{0,0} - \frac{2\Delta t}{\Delta z}(F^{0,1} - F^{0,0}) = \rho_d^{0,0} - \frac{2\Delta t}{\Delta z}(F^{0,1}), \quad (16)$$

where $F^{0,-1} = -F^{0,1}$ and $F^{0,0} = 0$. Equation (16) serves as the boundary condition for $z=0$.

At $z=3H$, the boundary condition is set as $\rho_d=0$ to reflect the negligible contribution of dust densities at such heights, as shown in Fig.3.

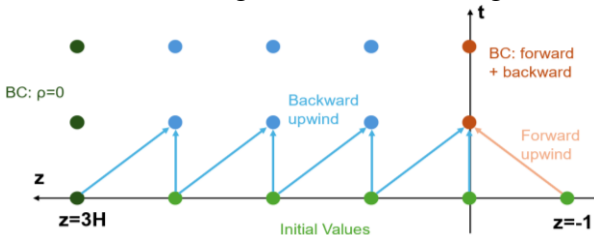


Fig.3. Computational approach of solving advection PDE. Blue dots and orange dots can be solved using Equation (15) and (16), respectively. Values at each discretized time point are computed iteratively from the previous time step.

B. Advection-Diffusion Situation

Using a similar approach as in the pure advection case, Equation (11) has a natural form:

$$\frac{\partial \tilde{\rho}_d}{\partial t} + \frac{\partial}{\partial z}(\tilde{u}_z \tilde{\rho}_d) - \alpha \frac{\partial}{\partial z} \left[\tilde{\rho}_g \frac{\partial}{\partial z} \left(\frac{\tilde{\rho}_d}{\tilde{\rho}_g} \right) \right] = 0. \quad (17)$$

All reference coefficients cancel out during the transformation. For the diffusion term, this leaves

only the dimensionless parameter α .

Diffusion propagates information symmetrically in both $+z$ and $-z$ directions, spreading from regions of high concentration to low concentration. Thus, central difference scheme is used as it captures this bidirectional nature of information flow. The inner derivative $\frac{\partial}{\partial z} \left(\frac{\rho_d}{\rho_g} \right)$, representing the dust-gas density ratio gradient, is first evaluated using central differences. For a grid point i , this is expressed as:

$$\frac{\partial}{\partial z} \left(\frac{\rho_d}{\rho_g} \right)_i = (\frac{\rho_d[i+1]}{\rho_g[i+1]} - \frac{\rho_d[i-1]}{\rho_g[i-1]})/2\Delta z. \quad (18)$$

The outer derivative is then evaluated as:

$$\frac{\partial}{\partial z} \left[\rho_g \frac{\partial}{\partial z} \left(\frac{\rho_d}{\rho_g} \right) \right]_i = ((\rho_g \cdot grad_{in})[i+1] - (\rho_g \cdot grad_{in})[i-1])/2\Delta z \\ = (\rho_g[i+1] \left(\frac{\rho_d[i+2]}{\rho_g[i+2]} - \frac{\rho_d[i]}{\rho_g[i]} \right) - \rho_g[i-1] \left(\frac{\rho_d[i]}{\rho_g[i]} - \frac{\rho_d[i-2]}{\rho_g[i-2]} \right))/4\Delta z^2 \quad (19)$$

However, when using whole grid points, the effective grid spacing is $2\Delta z$, which provides a resolution four times worse than a scheme that uses the optimal grid spacing of Δz . To refine the resolution, we can imagine a coarser grid with z -spacing twice that of the current grid. In this setup, the integer points $i \pm 1$ and $i \pm 2$ of the initial grid align with the midpoint locations $i \pm 1/2$ and $i \pm 3/2$ of the coarser grid. Thus, RHS of Equation (19) becomes:

$$= \frac{1}{\Delta z^2} \left[\rho_g \left[i + \frac{1}{2} \right] \left(\frac{\rho_d[i+1]}{\rho_g[i+1]} - \frac{\rho_d[i]}{\rho_g[i]} \right) - \rho_g \left[i - \frac{1}{2} \right] \left(\frac{\rho_d[i]}{\rho_g[i]} - \frac{\rho_d[i-1]}{\rho_g[i-1]} \right) \right], \quad (20)$$

Equation (20) is valid for any grid spacing Δz , therefore, it applies to the original grid as well.

Using linear interpolation to determine $\rho_g[1 \pm 1/2]$:

$$\frac{1}{\Delta z^2} \left[\frac{\rho_g[i] + \rho_g[i+1]}{2} \left(\frac{\rho_d[i+1]}{\rho_g[i+1]} - \frac{\rho_d[i]}{\rho_g[i]} \right) - \frac{\rho_g[i] + \rho_g[i-1]}{2} \left(\frac{\rho_d[i]}{\rho_g[i]} - \frac{\rho_d[i-1]}{\rho_g[i-1]} \right) \right], \quad (21)$$

serves as the diffusion contribution to point i .

Equation (21) can be separated into advection and diffusion contributions, as these processes are independent: advection depends solely on the velocity field, while diffusion depends on density gradients, therefore, $\rho_d^{n+1,i}$ can be computed as:

$$\rho_d^{n+1,i} = \rho_d^{n,i} + \Delta t(\alpha \cdot diff_{contribution} - adv_{contribution}). \quad (22)$$

Substituting the symmetry condition $\rho_d[-1] = \rho_d[1]$ into Equation (21) provides the diffusion contribution at the boundary $z=0$, enabling ρ_d at each time steps to be evaluated using Equation (22).

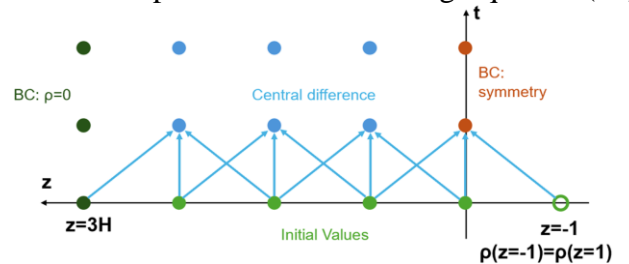


Fig.4. Computational approach of solving diffusion PDE. Blue dots and orange dots can both be solved by Equation (21) when symmetry condition is applied.

To evaluate the numerical stability, the diffusion term in Equation (17) is expanded as:

$$-\alpha \frac{\partial}{\partial z} \left[\bar{\rho}_g \frac{\partial}{\partial z} \left(\frac{\bar{\rho}_d}{\bar{\rho}_g} \right) \right] = -\alpha \frac{\partial^2 \bar{\rho}_d}{\partial z^2} + \alpha \frac{\partial}{\partial z} \left(\frac{\bar{\rho}_d}{\bar{\rho}_g} \cdot \frac{\partial \bar{\rho}_g}{\partial z} \right), \quad (23)$$

where the first term on the RHS serves as the main diffusion term with CFL condition $\Delta t \leq \Delta z^2 / 2\alpha$. The second term is a correction term due to the spatially varying ρ_g . We define an intrinsic length scale L_z where ρ_g undergoes significant changes. For a Gaussian, this is usually its standard deviation, which in our case is 1. Therefore, the order of magnitude of the inner derivative $\frac{\rho_d}{\rho_g} \frac{\partial \rho_g}{\partial z}$ is $\rho_d / \Delta z$, this order of magnitude is divided by Δz by evaluating its z derivative again. Thus, the order of magnitude of the correction term is:

$$\alpha \cdot \rho_d / (L_z \cdot \Delta z). \quad (24)$$

Compared to the main term's order of magnitude $\alpha \rho_d / \Delta z^2$, the correction term is smaller by $\Delta z / L_z$. Thus, for $\Delta z \ll 1$, numerical stability is still governed by the standard CFL. We set $\Delta z = 1/300$ to satisfy this, with $\Delta t = \Delta z^2 / 3\alpha$ chosen conservatively. The final timestep is the minimum of the advection and diffusion limits.

IV. RESULTS

A. Dust Settling

To determine the dust's settling timescale to the mid-plane under pure advection, the dust density is evolved for 3 Myrs. The initial dust density was set to $0.01\rho_g$, and during each iteration, the dust-to-gas ratio was calculated by dividing the updated dust density by the constant ρ_g array, as ρ_g only varies with z . The simulation stopped when the ratio at any position exceeded 1, indicating dust settling. This process was repeated for different radial distances R , recording the time required for the dust to settle at each location, as shown in Fig. 5.

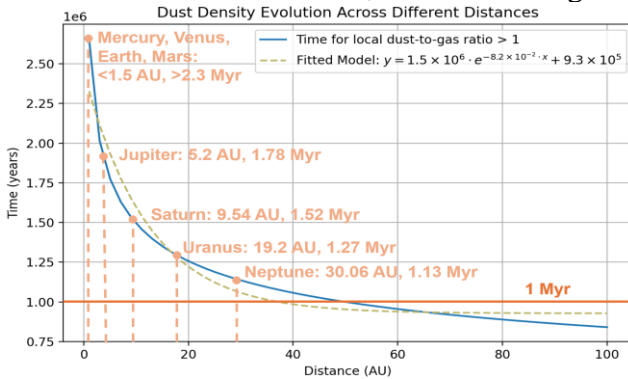


Fig.5. Time required for the local dust to settle against radial distance. The blue curve represents simulation results, and the dashed line shows an exponential fit. Key points for planets and discs' lifetime 1Myr are annotated.

The results indicate that the time for dust settling decreases approximately exponentially with radial

distance. For inner planets (Mercury, Venus, Earth, Mars, <1.5 AU), the timescale exceeds 2.3 Myr, far longer than the 1 Myr disc lifetime. Jupiter's timescale also exceeds 1 Myr by 78%, this suggests that additional mechanisms, such as dust particle growth, pressure bumps, or pebble accretion, were necessary to enable planetesimal formation at these distances [4]. For Saturn, Uranus, and Neptune, the settling times are slightly above 1 Myr, suggesting that planetesimal formation was possible but likely required additional processes. Beyond 50 AU, settling occurs within 1 Myr, as lower gas densities reduce drag and allow faster dust accumulation, favouring planetesimal formation.

B. Turbulent Diffusion of The Dust

Without turbulence, dust particles settle into a very thin layer at the mid-plane, as shown in Fig.8. However, turbulence creates an equilibrium where the downward gravitational force is balanced by the upward diffusion caused by turbulence, as shown in Fig.6. This results in the dust being distributed over a finite height above the mid-plane. To align the simulation results with the observation shown in Villenave et al. (2020) [5], where the dust settling height at $R \sim 100$ AU is around $z \sim 0.1R$, the parameter α must be determined to align this level of turbulence. A typical α is on the order of magnitude of 10^{-5} , 10^{-4} , or 10^{-3} [6], thus, advection-diffusion scenarios with these α values are simulated at $R=100$ AU.

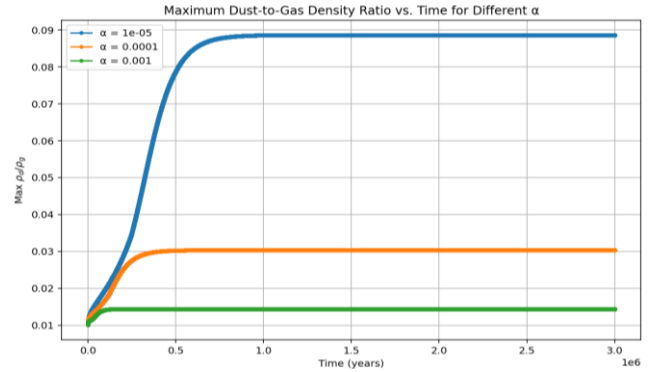


Fig.6. Maximum dust-to-gas density ratio over time for three different turbulent levels at $R=100$ AU.

This result indicates that the dust-to-gas density ratio reaches a steady-state equilibrium due to the balance between vertical settling and turbulent diffusion. The stronger the turbulence, the more the max density ratio is suppressed, resulting in a lower equilibrium value. For all tested α values, equilibrium is achieved below a dust-to-gas ratio of 0.1. This confirms that for $1 \mu m$ dust particles, turbulence prevents them from complete settling to the mid-plane regardless of the time. We then capture snapshots of the spatial distribution of the

density ratio to illustrate its evolution over time, with the maximum time set to 1.5 Myr, as the distribution stabilizes by this point.

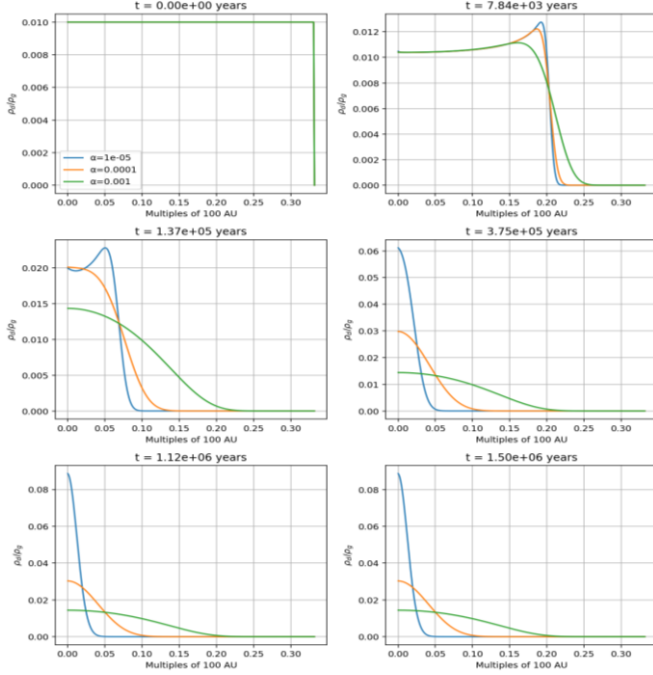


Fig.7. Six snapshots of the density ratio as a function of z at different times, scaled relative to multiples of 100 AU.

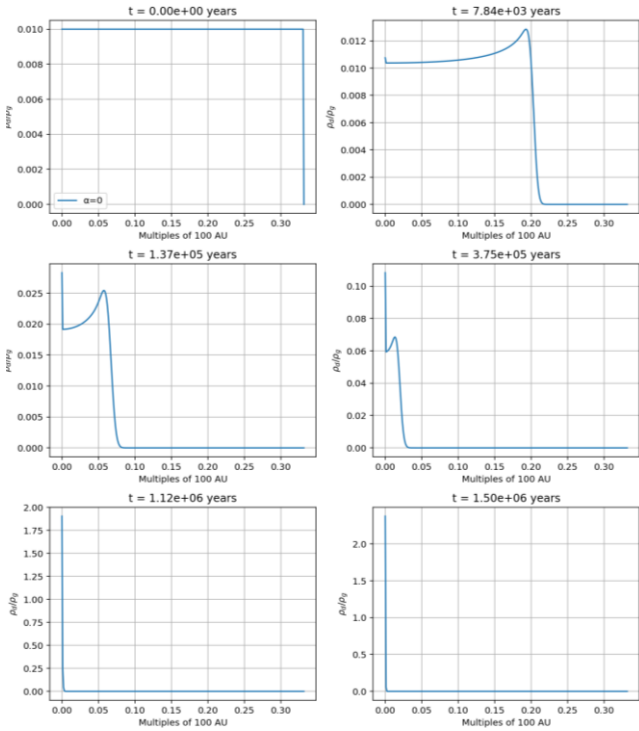


Fig.8. Snapshots of the density ratio as a function of z at different times for pure advection case ($\alpha=0$). $R=100$ AU

Over time, gravity drives dust toward the mid-plane, while turbulence redistributes it, which results in progressively narrower profiles as dust settles. The settling height, where the density ratio decreases significantly to almost zero, are evaluated for different α values. For $\alpha=10^{-5}$, weak turbulence leads to a settling height of approximately $z \sim 0.05R$, allowing dust to concentrate close to the mid-plane. For $\alpha=10^{-4}$,

moderate turbulence increases the settling height to $z \sim 0.1R$, aligning well with observations of dust distributions. For $\alpha=10^{-3}$, strong turbulence prevents significant settling, resulting in a broad dust distribution with a settling height of $z \sim 0.2R$. Therefore, we reach the conclusion of $\alpha = 10^{-4}$ to an order of magnitude accuracy.

Without turbulence, there is no vertical diffusion to counteract the gravitational force pulling dust particles toward the mid-plane. As a result, the dust layer becomes progressively thinner and more concentrated, creating a sharp increase in density ratio near $z=0$. Compared to cases with turbulence with broader profiles, the lack of turbulence results in highly concentrated dust near the mid-plane.

C. Dust Particle Growth

The velocity u_z , driven by the balance between gravitational force and drag, increases linearly with particle size. This means that larger particles settle faster, as they experience less drag relative to their inertia, making them possible to overcome turbulent diffusion and settle to the mid-plane.

Stabilization indicates that the system has reached its maximum possible value for density ratio. If this stabilized value remains below 1, it confirms that the particle size is insufficient to overcome turbulence and fully settle to the mid-plane. From Fig. 6, it is observed that changes in the stabilized maximum density ratio are smaller than 10^{-8} . Based on this, the simulation monitors the maximum density ratio across timesteps, and if the change over five consecutive timesteps is less than 10^{-8} , the system is considered stabilized, and the simulation terminates. This method allows us to quickly detect the critical particle size for dust settling, despite the increase in u_z decreases the time spacing and increases the computational cost. Fig.9. shows the results of critical sizes at distances of giant planets in the solar system.

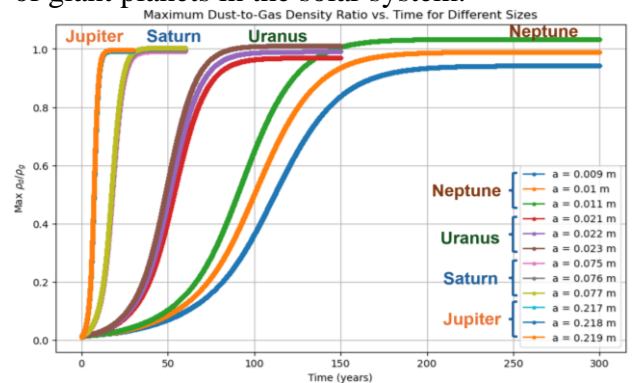


Fig.9. For each planet, the three particle sizes tested that are closest to achieving a density ratio of 1 are shown. The results are reported as the middle value \pm the resolution.

Particles closer to the Sun require larger sizes to overcome stronger turbulent diffusion and achieve a density ratio exceeding 1, as the gas density and turbulence are higher in the inner regions of the disc. Consequently, the equilibrium times for the density ratio to stabilize are shorter for larger particles near the Sun, reflecting faster settling dynamics. The critical particle sizes for each planet are as follows: Jupiter ($0.218 \pm 0.001 \text{ m}$), Saturn ($0.076 \pm 0.001 \text{ m}$), Uranus ($0.023 \pm 0.001 \text{ m}$) and Neptune ($0.010 \pm 0.001 \text{ m}$).

D. Numerical Diffusion

Reviewing Equation (15) and (21), we note that while the diffusion term is discretized using a second-order central difference method, the advection term employs a first-order upwind scheme. As a result, the advection term dominates the overall error, where it introduces a second-order numerical diffusion term, proportional to Δz .

In the absence of physical diffusion, gravitational settling cannot be counteracted, therefore the density ratio would increase without stabilization. However, the observed stabilization of the maximum density ratio over time with $\alpha=0$ indicates the presence of numerical diffusion. To further quantify this, we compared the effects of numerical diffusion with those of physical diffusion for different values of α , we also compare against different Δz , as shown in Fig.10.

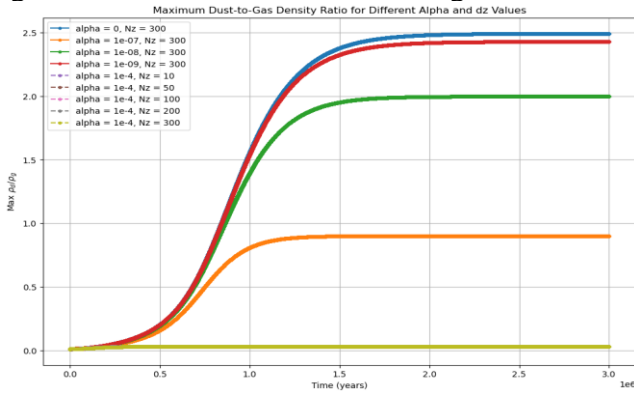


Fig.10. Maximum density ratio as against time for various α values and z grid numbers (N_z), $R=100$ AU. For $\alpha=10^{-4}$ the lowest golden line shows that results for different resolutions ($N_z=10, 50, 100, 300$) are almost identical, indicating convergence. For smaller α values, results depend on α . $\alpha=0$ case demonstrates pure numerical diffusion.

Therefore, for $\alpha=10^{-4}$ the system is fully governed by physical diffusion, as the curve stabilizes at a significantly lower density ratio, far from the influence of numerical diffusion. Even for the worst resolution ($N_z=10$), numerical diffusion is negligible and not comparable to the $\alpha=0$ case. This demonstrates that $N_z=300$ is a safe and robust choice. At $\alpha=10^{-7}$, smaller times begin to exhibit

numerical diffusion effects, and for $\alpha=10^{-9}$, the numerical diffusion becomes entirely comparable to physical diffusion. As $\alpha=10^{-4}$ is 5 orders of magnitude lower than $\alpha=10^{-9}$, we are reassured that the physical diffusion in the cases we analyze is robustly unaffected by numerical artifacts.

V. CONCLUSION

This study reveals that the settling time decreases with increasing radial distance, suggesting that planets in the Solar System are unlikely to form under $1 \mu\text{m}$ dust conditions within the disc's lifetime. The turbulent strength $\alpha=10^{-4}$ was determined, parallel to the observation. Initial tests confirmed that $1 \mu\text{m}$ particles cannot settle due to turbulent diffusion. Subsequent simulations identified the minimum particle size required for settling at the orbits of the giant planets. These values cannot be verified as no literature was found for direct comparison, but the observed trends are consistent with theoretical expectations and can be explained by the combined effects of turbulent diffusion and gravitational settling.

The robustness of these results is further supported by numerical convergence tests, which ensure that the findings are not influenced by resolution or numerical diffusion. Given these factors, we choose to accept the results as a reliable representation of the conditions required for planetesimal formation.

Future improvements could involve exploring higher-order advection schemes and incorporating more detailed dust growth and collision processes to provide deeper insights into planet formation.

REFERENCES

- [1] ALMA Observatory, "Revolutionary ALMA image reveals planetary genesis," [Online]. Available: <https://www.almaobservatory.org/en/press-releases/revolutionary-alma-image-reveals-planetary-genesis/>. [Accessed: 13-Dec-2024].
- [2] A. Fick, "Ueber Diffusion," *Annalen der Physik*, vol. 170, no. 1, pp. 59–86, 1855. DOI: 10.1002/andp.18551700105.
- [3] N. I. Shakura and R. A. Sunyaev, "Black holes in binary systems. Observational appearance," *Astronomy & Astrophysics*, vol. 24, pp. 337–355, 1973.
- [4] A. Johansen and A. Youdin, "Protoplanetary Disk Turbulence Driven by the Streaming Instability: Nonlinear Saturation and Particle Concentration," *The Astrophysical Journal*, vol. 662, no. 1, pp. 627–641, 2007. DOI: 10.1086/516730.
- [5] M. Villenave, *et al.*, "High-resolution imaging of planet formation regions," *Astronomy & Astrophysics*, vol. 642, p. A164, 2020. DOI: 10.1051/0004-6361/202038087.
- [6] L. Hartmann, N. Calvet, E. Gullbring, and P. D'Alessio, "Accretion and the Evolution of T Tauri Disks," *The Astrophysical Journal*, vol. 495, no. 2, pp. 385–400, 1998. DOI: 10.1086/305277.